Relationship between optimal precursors for Indian Ocean Dipole events and optimally growing initial errors in its prediction

Mu Mu[1], Rong Feng[2] (ID)**, and Wansuo Duan[2,3]** (ID)

[1]Institute of Atmospheric Sciences, Fudan University, Shanghai, China, [2]LASG, Institute of Atmospheric Physics, Chinese Academy of Sciences, Beijing, China, [3]University of Chinese Academy of Sciences, Beijing, China

Abstract Using the Geophysical Fluid Dynamics Laboratory Climate Model version 2p1, we explored the precursory disturbances that are most likely to develop into a positive Indian Ocean Dipole (IOD). The dominant spatial patterns of these precursors are defined as the optimal precursors (OPRs) of positive IOD as they are more inclined to cause a positive IOD than other superimposed initial perturbations in the experiments. Specifically, there are two types of OPRs with opposite patterns; the surface component of OPR-1 (OPR-2) is an indistinctive west-east dipole pattern, with a small area of negative (positive) perturbations to the coast of Sumatra and Java. Correspondingly, there is a significant west-east dipole pattern in the subsurface component of the OPRs, with the largest values located in the eastern equatorial Indian Ocean. The dominant mode of the time-dependent evolutions of the precursors features rapid development of positive IOD. Furthermore, the OPRs are similar to the optimally growing initial errors (OGEs) associated with IOD predictions that have been presented in previous studies. The shortwave radiation, latent heat flux, and westward Rossby waves play an important role in the time-dependent evolution of OGEs. Moreover, the large values of the OPRs are located in the same areas as the sensitive areas of targeted observations identified by the OGEs. This infers that intensive observations over these areas would not only reduce initial errors, improve the accuracy of initial fields and decrease the prediction errors but would also detect the precursory signals in advance, which substantially improves the forecast skill of IOD.

1. Introduction

Tropical oceans play an important role in regulating the global climate variability. The El Niño-Southern Oscillation (ENSO), which is the dominant phenomenon of interannual time scale in the tropical Pacific Ocean, has been studied for decades [*Rasmusson and Carpenter*, 1982; *Philander*, 1983, 1990]. However, the Indian Ocean Dipole (IOD), a well-known ocean-atmosphere coupled phenomenon of interannual time scale in the tropical Indian Ocean, has only received attention in recent years [*Saji et al.*, 1999; *Webster et al.*, 1999]. The positive mode of the IOD presents positive sea surface temperature anomalies (SSTAs) in the western Indian Ocean and negative SSTAs in the eastern Indian Ocean, accompanied by an anomalous easterly wind [*Saji et al.*, 1999; *Webster et al.*, 1999; *Li et al.*, 2002, 2003]. Corresponding to this seesaw pattern in the SSTAs, a west-east dipole pattern is present in the sea temperature anomalies of the subsurface ocean [*Rao et al.*, 2002; *Feng and Meyers*, 2003]. In contrast, the negative IOD has the opposite sea temperature and wind anomalies. The IOD can regulate the monsoons and thus affect the climate and weather of nearby regions, such as eastern Africa, Indonesia and Australia [*Ansell et al.*, 2000; *Black et al.*, 2003; *Zubair et al.*, 2003; *Behera et al.*, 2005]. Moreover, IOD can also affect distant areas, such as Europe, Northeast Asia, North America, South America, and South Africa, by the propagation of planetary waves [*Guan and Yamagata*, 2003; *Saji and Yamagata*, 2003]. *Zhang et al.* [2015] demonstrated that in the positive IOD, abundant rain shifts from the tropical regions to the south of China through northern India, the Bay of Bengal and Southeast Asia in positive IOD. Conversely, the severe droughts shift to the south of China through these regions in the negative IOD. In consideration of the considerable climatic effects of IOD events on nearby and distant areas, it is vital to accurately predict IOD events.

Many studies have shown that the lead time for skillful IOD predictions is only one season, and this can be prolonged to two seasons for strong IOD events [*Wajsowicz*, 2004, 2005; *Luo et al.*, 2005, 2007; *Zhao and*

Hendon, 2009; *Shi et al.*, 2012, *Liu et al.*, 2016]. Furthermore, the low forecast skill may have a close relationship with the winter predictability barrier (WPB). From the viewpoint of statistics, the WPB means that whatever the start month, the forecast skill decreases rapidly across the boreal winter [*Luo et al.*, 2007]; from the viewpoint of initial error growth, the WPB indicates that the prediction errors present the largest growth in boreal winter [*Feng and Duan*, 2014; *Feng et al.*, 2016]. As the composite dipole mode index (DMI) for the positive IOD generally reverses its sign in both the winter preceding the IOD year and in the IOD year [*Wajsowicz*, 2004; *Feng et al.*, 2014a], indicating the occurrence and decay of positive IOD, the existence of the WPB probably constrains the forecast skill for the occurrence and decay of a positive IOD. *Feng et al.* [2016] demonstrated that the dominant spatial pattern of initial sea temperature errors that are most likely to cause a significant WPB for positive IOD (hereafter referred to as WPB-related initial errors) presents a west-east dipole pattern in the tropical Indian Ocean, especially in the subsurface ocean. In addition, the areas in which the large values of the dominant spatial pattern are located (i.e., at the thermocline depth in the eastern equatorial Indian Ocean) represent the sensitive areas of targeted observations for positive IOD. We therefore need to determine how these WPB-related initial errors develop and cause large prediction errors. Consequently, the physical mechanisms of development for these initial errors are further discussed in this study.

Apart from the aforementioned WPB-related initial errors, the precursor is another important issue in the predictability of the positive IOD. The precursor for positive IOD refers to the initial perturbations that develop into a positive IOD. The study of the precursor is important for identifying the IOD in advance and therefore improving the forecast skill. Based on buoy data during 2006–2008, *Horii et al.* [2008] showed that there were significant negative signals at the thermocline depth in the eastern equatorial Indian Ocean several months prior to the appearance of the SSTAs, and these negative signals are the precursor of the positive IOD. This leads to the question of whether or not all positive IOD events have the same precursor.

Previous studies showed that there is a great spatial similarity between the optimally growing initial errors (OGEs) and optimal precursors (OPRs) in the predictability of blocking onset [*Mu and Jiang*, 2011], ENSO [*Mu et al.*, 2014; *Hu and Duan*, 2016], Kuroshio large meander (KLM) [*Wang et al.*, 2013], and the North Atlantic Oscillation [*Dai et al.*, 2016], and the large values of the OGEs and OPRs are located within small areas. These areas have been demonstrated to be the sensitive areas for targeted observations for these events [*Mu and Jiang*, 2011; *Wang et al.*, 2013; *Mu et al.*, 2014; *Hu and Duan*, 2016]. Therefore, intensive observations carried out over these areas will not only improve the accuracy of the initial fields and further decrease the prediction errors, but also detect the precursory signals in advance, which will substantially improve the forecast skill for these events. Therefore, this inspires us to determine the probable relationship between the OGEs and OPRs corresponding to a positive IOD. In this study, as positive IOD events have larger climate effects and more frequent occurrence under climate change conditions than negative events [*Ashok et al.*, 2001, 2003; *Abram et al.*, 2003; *Annamalai and Murtugudde*, 2004; *Behera et al.*, 2005; *Cai et al.*, 2009; *Weller and Cai*, 2013], only positive IOD events are discussed.

The remainder of the paper is organized as follows. The model and experimental strategy are presented in section 2. The spatial patterns of the OPRs and OGEs, and their physical development mechanisms, are discussed in section 3. The similarities between the OPRs and OGEs are analyzed in section 4. A summary and discussion is presented in the last section.

2. Model and Experimental Strategy

In this study, the Geophysical Fluid Dynamics Laboratory Climate Model version 2p1 (GFDL CM2p1) was used to explore the OPRs and OGEs of the positive IOD. The model contains an ocean component, an atmospheric component, a land component, and a sea ice component. We will briefly introduce the coupled model below, and for more details, please refer to *Griffies* [2009] and *GFDL Global Atmospheric Model Development Team* [2004].

The ocean component of the coupled model is the Modular Ocean Model version 4 (MOM4p1) [*Griffies*, 2009], which is a numerical representation of the ocean's hydrostatic primitive equations. Its horizontal resolution is $1° \times 1°$ in most regions and its meridional resolution reduces to $1/3°$ near the equator. In total, there are 50 levels in the vertical, with a resolution of 10 m in the upper 225 m. The atmospheric component of the coupled model is the GFDL atmospheric model AM2p12b [*GFDL Global Atmospheric Model*
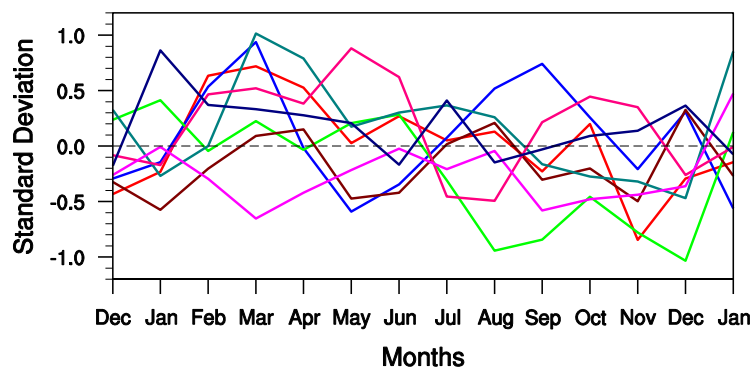
Figure 1. Time-dependent DMIs for each neutral year. The colorful lines represent eight neutral years.

Development Team, 2004], and it has a resolution of 2.5° longitude by 2° latitude with 24 vertical levels. The different components are coupled using the GFDL's Flexible Modeling System (http://www.gfdl.noaa.gov/fms) and exchange the fluxes every 2 h. *Feng et al.* [2014b] assessed the simulation ability of this coupled model in terms of the climatology in the tropical Indian Ocean and the basic characteristics of the IOD, and found that this model has high simulation skill. Therefore, the GFDL CM2p1 is appropriate to study the predictability of the IOD.

In previous studies, the conditional nonlinear optimal perturbation (CNOP) [*Mu et al.*, 2003] approach has been applied to explore the OPRs of ENSO [*Mu et al.*, 2014] and KLM [*Wang et al.*, 2013]. The CNOP represents the optimal initial perturbation that has the largest nonlinear evolution at the end of the optimization and is an extension of a linear singular vector in a nonlinear regime. Generally speaking, the adjoint model provides an efficient tool for the calculation of the gradient, which is needed for some optimization algorithms, e.g., spectral projected gradient 2. However, the adjoint model is not a necessary condition for the gradient calculations; for example, the gradient can be calculated directly in low-dimensional nonlinear optimization problems [*Mu et al.*, 2003]. In high-dimensional models (e.g., the GFDL CM2p1), there are generally no adjoint models and it is also difficult to calculate the gradient directly. Therefore, other approaches should be developed to calculate the OPRs in complex models. *Duan et al.* [2009] proposed an ensemble-based algorithm to calculate CNOP approximately without using the adjoint models. By applying this approach, they explored the OPRs of ENSO in the Zebiak-Cane model and their results were demonstrated to be reasonable and similar to those calculated with the adjoint models. Therefore, this ensemble-based algorithm offers a practical method to extend the basic idea of CNOP to complex coupled models. In this study, we will explore the OPRs of positive IOD with the algorithm proposed by *Duan et al.* [2009]. The remainder of this section provides details of our experimental strategy.

The GFDL CM2p1 was integrated for 150 years under the 1990 forcing values of aerosols, land cover, tracer gases, and insolation. We only analyzed the last 100 years to exclude the effect of initial adjustment process during the initial 50 year spin-up. To explore the precursors of positive IOD, we randomly selected eight neutral years from the 100 year integration as a reference state (Figure 1). Here "neutral years" indicate that no positive IOD or negative IOD occurs in these years; that is, the DMI (i.e., the difference in SSTA between the western Indian Ocean (50°E–70°E, 10°S–10°N) and southeastern Indian Ocean (90°E–110°E, 10°S–equator)) [*Saji et al.*, 1999] does not satisfy the following condition: the absolute value of the DMI exceeds 0.5 standard deviations for three consecutive months [*Song et al.*, 2007].

Assuming that the initial perturbations occurred in the sea temperature, the initial perturbations that develop into positive IOD (i.e., precursors) computed in the GFDL CM2p1 only have a sea temperature component. In consideration of the 4 year period of IOD events in the GFDL CM2p1 [*Feng and Duan*, 2014], which indicates that a positive IOD and a negative IOD usually occur within 4 years, sea temperature anomalies within the 4 years preceding each neutral year (i.e., reference year) are various and sampled every month to ensure that initial perturbations were as plentiful as possible. Therefore, there were a total of 48 initial perturbations for each reference year. As the mean thermocline depth is about 110–130 m in the tropical Indian Ocean [*Song et al.*, 2007], the perturbations on the sea temperature at 95 m depth could reflect the variation of the thermocline depth to some extent. Moreover, the sea surface temperature (SST) is an important variable that closely connects the ocean and the atmosphere. In view of the fact that initial shock probably happens when all levels of sea temperatures are perturbed in the tropical Indian Ocean, perturbations were only superimposed on the sea temperatures at the sea surface and at 95 m depth in the tropical

Indian Ocean (45°E–115°E, 10°S–10°N), which are closely related to the evolution of IOD events [*Rao et al.*, 2002; *Vinayachandran et al.*, 2002]. Furthermore, to impartially compare the effects of different initial perturbations on the predictability of positive IOD, we adjusted them into the same magnitude. As the DMI of positive IOD generally reverses its sign in the winter preceding the IOD year [*Wajsowicz*, 2004; *Feng et al.*, 2014a], which indicates the occurrence of the positive IOD, the start month of the integrations were defined as December in the preceding year of reference year (i.e., December (−1), where −1 denotes the year preceding the reference year). We then superimposed these initial perturbations onto the initial fields of the reference year and integrated them from December (−1) for 12 months. Therefore, we conducted 384 predictions in total (8 neutral years multiplied by 48 initial perturbations). Based on these 384 predictions, we explored the initial perturbations that are most likely to develop into positive IOD.

The detailed steps were as follows. The original initial perturbations at the sea surface and 95 m depth were labeled as T_1 and T_2, respectively. T_{1ij} and T_{2ij} indicate the values of T_1 and T_2 at gridpoint (i, j) in the tropical Indian Ocean (i.e., 10°S–10°N, 45°E–115°E). Then T_1 and T_2 were scaled to the same magnitude by $T'_1 = T_1/\delta_1$ and $T'_2 = T_2/\delta_2$, where δ_1 and δ_2 represent positive values which are chosen to ensure the same magnitude between T'_1 and T'_2, and T'_1 and T'_2 are the final initial perturbations superimposed on the reference states. The magnitudes of these initial perturbations are constrained by the norms $\|T'_1\| = \sqrt{\sum_{i,j}(T'_{1ij})^2}$ and $\|T'_2\| = \sqrt{\sum_{i,j}(T'_{2ij})^2}$, which were set as 8°C in our study. The set of the magnitude ensures that the DMI of these initial perturbations were smaller than 0.5 standard deviations, and thus ensures that no positive IOD occurs at the start time of the predictions.

The experimental strategy to explore the initial errors that are most likely to cause a significant WPB (i.e., WPB-related initial errors) was similar to the above and is therefore only briefly described here. Please refer to *Feng et al.* [2016] for further details. The main difference from above experiments is that 10 positive IOD were randomly selected as the reference states (i.e., reference years) to explore the WPB-related initial errors instead of the neutral years. Sea temperature anomalies within the 4 years preceding each positive IOD were then sampled every other month to generate plentiful initial errors. In addition, another significant difference is that the start months here were defined as July (−1), October (−1), January (0), April (0), July (0), and October (0) where −1 denotes the year preceding the reference year, and 0 denotes the reference year; the reference year here refers to the IOD year. The integrations starting from the first three months bestride the winter in the growing phase of positive IOD, and those from the next three months bestride the winter in the decaying phase. After the 12 month integration, initial errors that grow fastest in winter and cause a significant WPB were selected and analyzed.

3. OPRs That Trigger IOD Onset and OGEs in IOD Predictions

In this section, according to the experimental strategy described in section 2, we explore the spatial patterns and physical development mechanisms of OPRs for the positive IOD. Similarly, the spatial patterns and the physical development mechanisms for OGEs are also discussed.

3.1. Spatial Patterns of OPRs That Trigger IOD Onset

As described in section 2, 384 predictions were conducted to explore the initial perturbations that develop into the positive IOD. After the 12 month integration, the sea temperature departure of the predictions from the reference state were considered to be the development of the initial perturbations. Here the predicted DMI was defined as the difference of sea surface temperature anomalies between the western Indian Ocean (50°E–70°E, 10°S–10°N) and eastern Indian Ocean (90°E–110°E, 10°S–equator). The SSTAs were calculated by subtracting the SST in the reference year from the corresponding predicted SST. If the predicted DMI exceeds 0.5 standard deviations for three consecutive months, a positive IOD occurs. That is, the corresponding initial perturbation superimposed on the initial fields of the reference state develops into a positive IOD and therefore could be considered a precursor of a positive IOD. According to this criterion, 31 initial perturbations developed into positive IOD and were selected as the precursors of positive IOD. Figure 2 shows the time-dependent DMI for these precursors. Most of the predicted positive IOD develop quickly in summer, peak in autumn, and then decay rapidly in winter. These phase locking characteristics are consistent with previous observational results [*Wajsowicz*, 2004]. To identify the spatial characteristics of these precursors, we applied the combined empirical orthogonal function (CEOF)
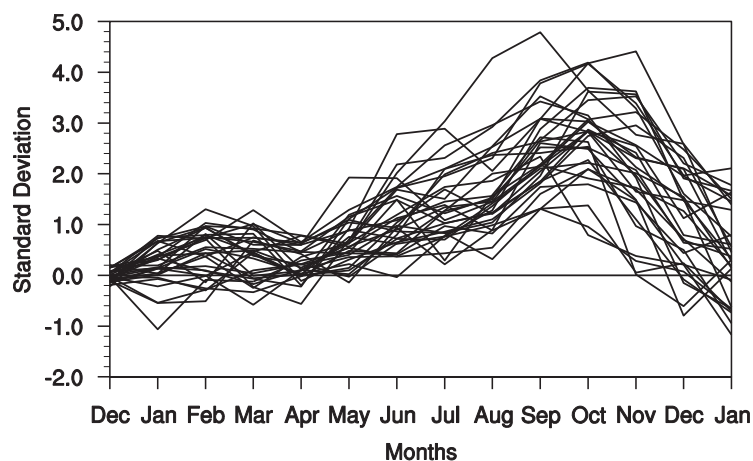
Figure 2. Time-dependent DMIs of each individual. The black lines represent 31 initial perturbations that develop into the positive IOD.

analysis to these 31 precursors, and the leading mode (i.e., CEOF1) describes their dominant spatial patterns. In consideration that these precursors are more inclined to develop into positive IOD than other superimposed initial perturbations in the experiments, and that the CEOF1 mode describes the dominant spatial patterns of these precursors, we defined the CEOF1 mode as the OPRs for the following discussions.

Figure 3 shows the spatial patterns of the CEOF1 mode (i.e., OPRs) and the corresponding time series (i.e., PC1). The CEOF1 mode accounted for 30.4% of the total variance in the tropical Indian Ocean. The surface component of the OPRs presents an indistinctive west-east dipole pattern with positive values located in most regions of the tropical Indian Ocean and a small area of negative values located at the coast of the Sumatra and Java. Unlike the surface component, the subsurface component presents a significant west-east dipole pattern, with positive values in the western Indian Ocean and negative values in the eastern Indian Ocean. The values in the subsurface component of the OPRs are generally larger than those in the surface component, with the largest values located in the eastern equatorial Indian Ocean. It is worth noting that the time series PC1 has both positive and negative values. Therefore, we can infer that some precursors have similar spatial patterns to the CEOF1 mode (hereafter referred to as OPR-1 for positive IOD), while other precursors have opposite spatial patterns to the CEOF1 mode (hereafter referred to as OPR-2). The spatial patterns of OPR-1 for positive IOD are consistent with the results of *Horii et al.* [2008], which demonstrated that negative signals at the thermocline depth in the eastern equatorial Indian Ocean are one precursor of positive IOD. Therefore, the above results indicate that there is also another type of OPR, in addition to the precursor revealed in *Horii et al.* [2008], that presents the opposite spatial patterns.

3.2. Possible Physical Mechanisms for Precursors of Positive IOD

The analysis in section 3.1 explored the dominant mode of the initial perturbations that develop into positive IOD (i.e., OPRs). In this section, we further analyze the dominant mode of the time-dependent evolutions for these precursors by applying season-reliant empirical orthogonal function (S-EOF) analysis [*Wang and An*, 2005]. The departure of the predicted sea temperatures from the corresponding reference states was considered as the development of precursors, which is 12 months in length and corresponds to a lead time of 12 months of predictions. We connected all the time-dependent series for 31 predictions and regarded them as a time series of year-to-year variations. We divided each year into six parts and examined the sea temperature anomalies in a sequence beginning from December (−1), January (0), to the following October (0), November (0), i.e., D(−1)J(0), FM(0), AM(0), JJ(0), AS(0), ON(0), where −1 denotes the year preceding the reference year and 0 denotes the reference year. The reference years here refer to the eight neutral years. This is a little different from the method of *Wang and An* [2005], which examines the SSTAs in a seasonal sequence. We then constructed a covariance matrix by treating the sea temperature anomalies in the above sequence as an integral block for 1 year. When the S-EOF analysis was performed, the derived spatial patterns for each S-EOF mode contained six sequential patterns. The different spatial patterns for each S-EOF mode describe the time-dependent evolutions of the sea temperature anomalies in a given year, which share the same yearly value in the corresponding time series PC.

By applying the S-EOF analysis to the SSTAs and vertical section (averaged between 5°S and 5°N) of sea temperature anomalies in the tropical Indian Ocean for 31 precursors, we identified the major modes of the time-dependent evolutions for the precursors (i.e., the first mode of S-EOF) and the corresponding time series PC1, which accounts for 22.5% and 33.9% of the total variance, respectively (Figure 4). We found that there are
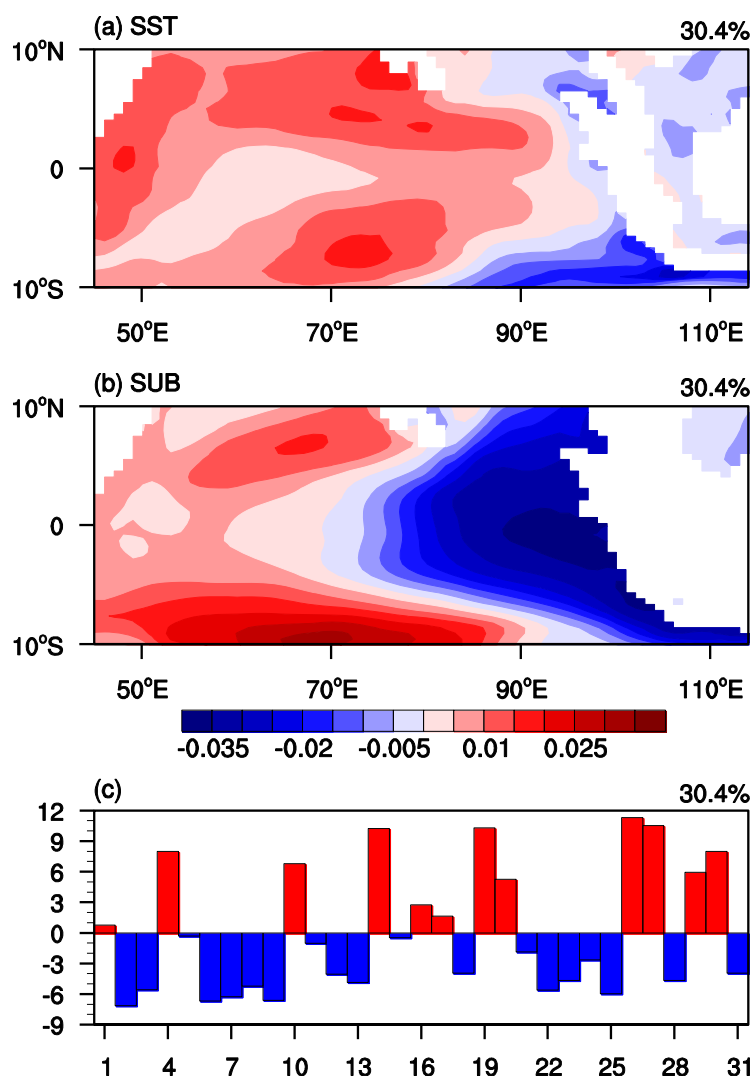
Figure 3. Spatial patterns of (a) surface component and (b) subsurface component for the leading mode of the combined empirical orthogonal function analysis of initial perturbations that are most likely to develop into the positive IOD (units: °C); (c) the corresponding time series PC1. The numbers located on the horizontal axis in Figure 3c represents the 31 predictions with different initial perturbations. Each number corresponds to one prediction.

positive SSTAs in the western Indian Ocean and negative SSTAs in the eastern Indian Ocean in the first 2 months of the predictions (Figure 4a). The distribution of SSTAs in the tropical Indian Ocean is favorable for the appearance of anomalous easterly wind at the equator, which further amplifies the negative SSTAs in the eastern Indian Ocean under the Bjerknes positive feedback in the following months [*Bjerknes*, 1969]. Meanwhile, the positive SSTAs gradually disappear and then reappear in the western Indian Ocean, finally resulting a significant west-east dipole pattern in the tropical Indian Ocean in October (0) and November (0). This indicates that the dominant evolution mode of SSTAs features a development of positive IOD. Accordingly, the evolution of the vertical sections shows that the negative temperature anomalies develop and amplify under the Bjerknes positive feedback in the eastern Indian Ocean, and finally develop into the positive IOD, which is consistent with the evolution of the SSTAs. Furthermore, the PC1s in Figures 4g and 4n show that the values are positive for most cases, indicating that most precursors develop in a similar behavior to Figure 4. That is, the evolution mode of most precursors feature a development of the positive IOD. However, it has been demonstrated that there are two types of OPRs for positive IOD. Do both types of OPRs develop in a similar behavior to Figure 4? To further answer this question, we divided the 31 precursors into two categories according to the sign of the PC1 in Figure 3 and explored the composite evolution mode for each category (not shown). It is found that the composite evolution mode of OPR-1 features a development of the positive IOD. For OPR-2, the SSTAs disappear rapidly in the first two months; then an opposite SSTA pattern appears which is similar to OPR-1. In the following months, this composite evolution mode presents a development of the positive IOD. That is, except for the first few months, the evolution mode of OPR-2 is similar to that of OPR-1. As the S-EOF method is applied to obtain the dominant evolution mode for precursors, the first mode of S-EOF generally only features a development of positive IOD.

3.3. Spatial Patterns of OGEs That Associated With a Significant WPB

Previous sections identified two types of OPRs and analyzed their time-dependent evolution with S-EOF analysis. In this section, we further discuss another important issue in the predictability for positive IOD from the viewpoint of initial error growth: the WPB-related initial errors. As *Feng et al*. [2016] has previously
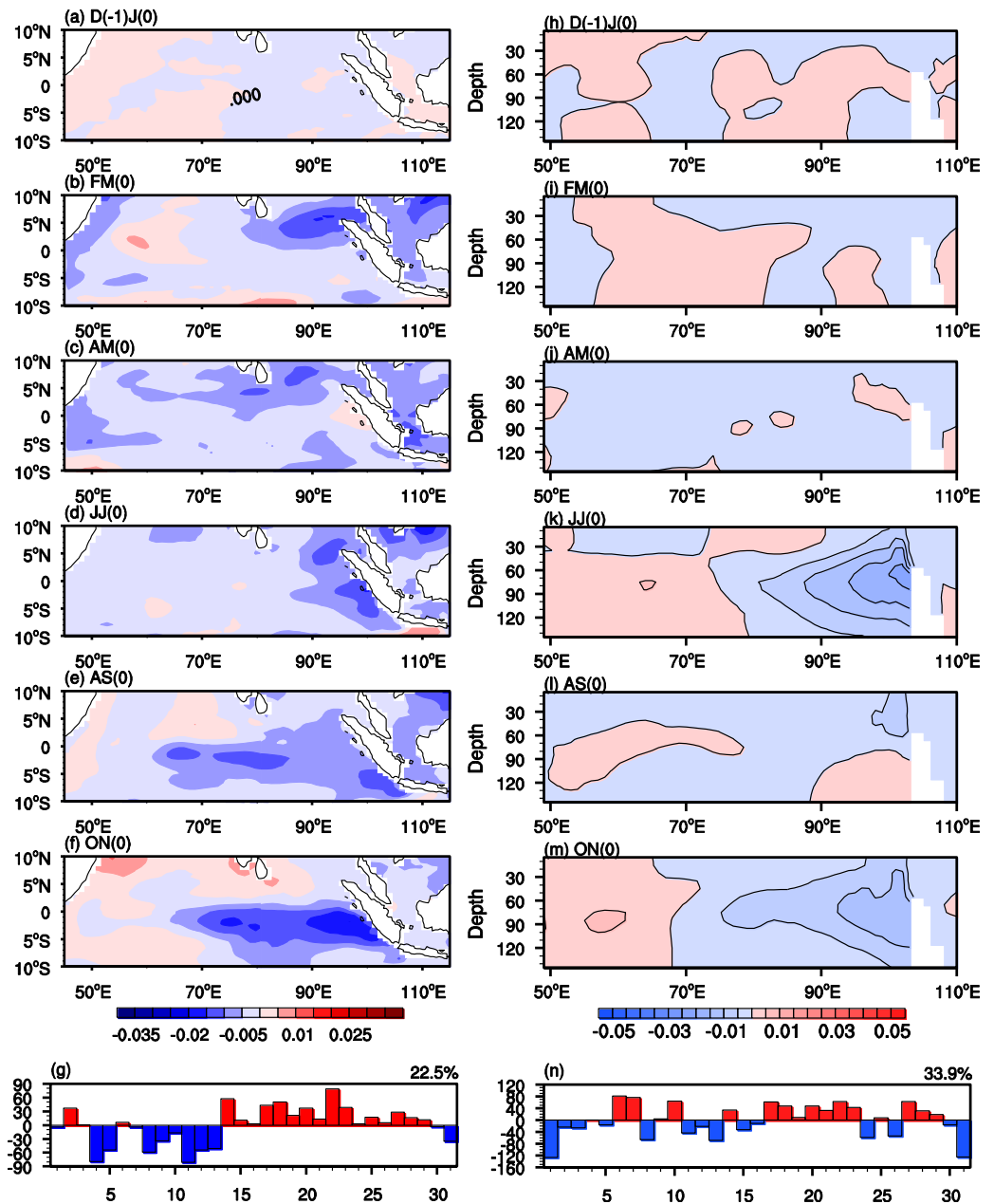
Figure 4. Major mode of time-dependent evolutions of (a–f) SSTAs and (h–m) equatorial (5°S–5°N) subsurface temperature anomalies for 31 initial perturbations (units: °C); (g and n) corresponding time series PC1. The horizontal axis in Figures 4g and 4n are as in Figure 3.

described the experimental strategy on how to explore the WPB-related initial errors, we only briefly state the results below.

As stated in section 1, *Feng et al.* [2016] explored the dominant spatial patterns of WPB-related initial errors with the CEOF analysis. As the WPB-related initial errors are more likely to cause a significant WPB than other super-imposed initial errors in the experiment and the CEOF1 mode of the WPB-related initial errors describes their dominant spatial patterns, we refer to the CEOF1 mode as OGEs in the following discussions. Due to the similarity of the results for the six start months, only the integrations starting from July (−1) and July (0) are illustrated in this section, which bestride the winter in the growing and decaying phases of positive IOD, respectively.

Figure 5 shows the spatial patterns of the OGEs and the corresponding time series PC1 for start months July (−1) and July (0). The CEOF1 mode accounted for 36.8% (38.0%) of the total variance in the tropical Indian Ocean for the start month July (−1) (July (0)). We found that the CEOF1 mode presents a west-east dipole
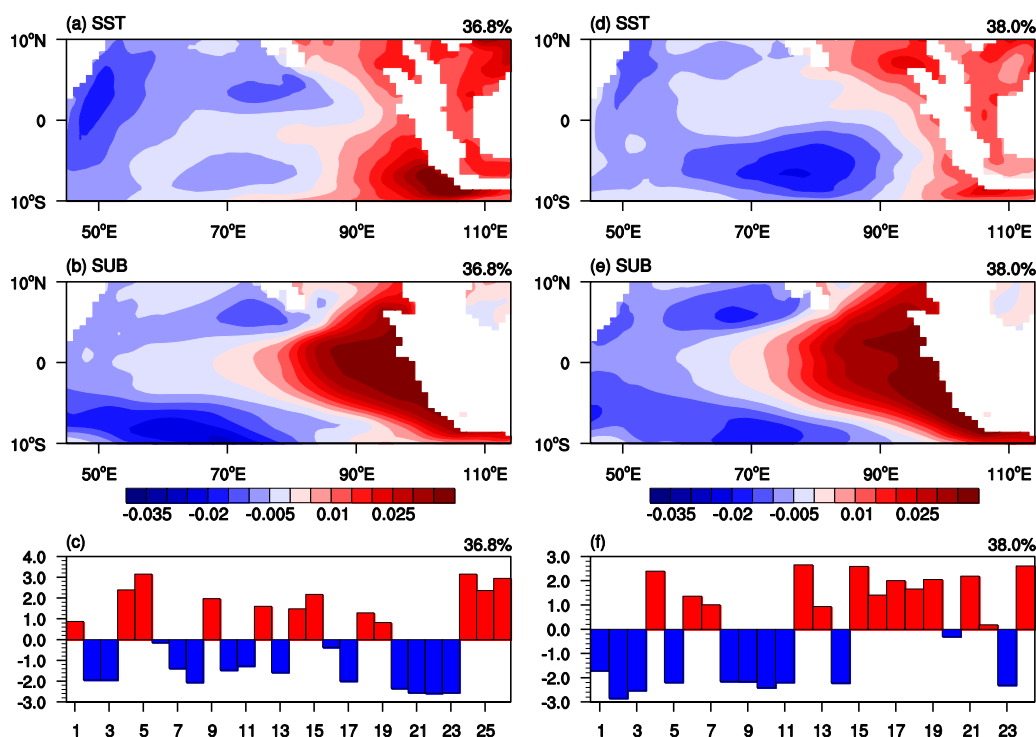
Figure 5. Spatial patterns of the (a) surface component and (b) subsurface component for the leading mode of the combined empirical orthogonal function analysis of initial errors that are most likely to cause a significant WPB for start month July (−1); (d and e) for the start month July (0) (units: °C). (c and f) the corresponding time series PC1. The numbers located on the horizontal axis in Figures 5c and 5f represents the 26 and 24 predictions with initial errors superimposed for start month July (−1) and July (0), respectively. Each number corresponds to one prediction.

pattern in both the surface and the subsurface components for start months July (−1) and July (0). The extrema in the subsurface component are larger than those in the surface component, with the largest values trapped in the eastern equatorial Indian Ocean. Moreover, the time series PC1 for start months July (−1) and July (0) have both positive and negative values, and this indicates that some WPB-related initial errors have a similar spatial pattern to the CEOF1 mode (hereafter referred to as OGE-1 for positive IOD), and some other WPB-related initial errors have the opposite spatial pattern to the CEOF1 mode (hereafter referred to as OGE-2 for positive IOD). Therefore, there are two main types of OGEs for both start months July (−1) and July (0), and these two types of OGEs have opposite spatial patterns. These characteristics of OGEs are similar to those of OPRs. In addition, the spatial patterns of the OGEs are also similar to those of the OPRs with a significant west-east dipole pattern in the subsurface component. One difference, however, is that the west-east dipole patterns are more apparent in the surface component of OGEs than that of OPRs. Previous studies have demonstrated that the great spatial similarity between the OPRs and OGEs provides information for identifying the sensitive areas of targeted observations for these events, which are favorable for improving the forecast skill [*Wang et al.*, 2013; *Mu et al.*, 2014; *Hu and Duan*, 2016]. Therefore, we further discuss the spatial similarity between the OPRs and OGEs and explore their application to the targeted observations of positive IOD in section 4.

3.4. Possible Physical Mechanisms for WPB-Related Initial Errors of Positive IOD

Feng et al. [2016] only explored the dominant spatial patterns of the WPB-related initial errors and did not discuss how these initial errors cause a WPB. In this section, we analyze the dominant evolution mode of these initial errors with the S-EOF analysis based on the work of *Feng et al.* [2016].

There are 26 (24) WPB-related initial errors for start month July (−1) (July (0)). Therefore, there are a total of 50 initial errors that are most likely to cause a significant WPB for these two start months. With the 12 month integration, the departure of the predictions from the reference state IOD events are considered as the development of these WPB-related initial errors. By conducting the S-EOF analysis to the SST errors and the vertical section (5°S–5°N) of the sea temperature errors in the tropical Indian Ocean for these 50 WPB-
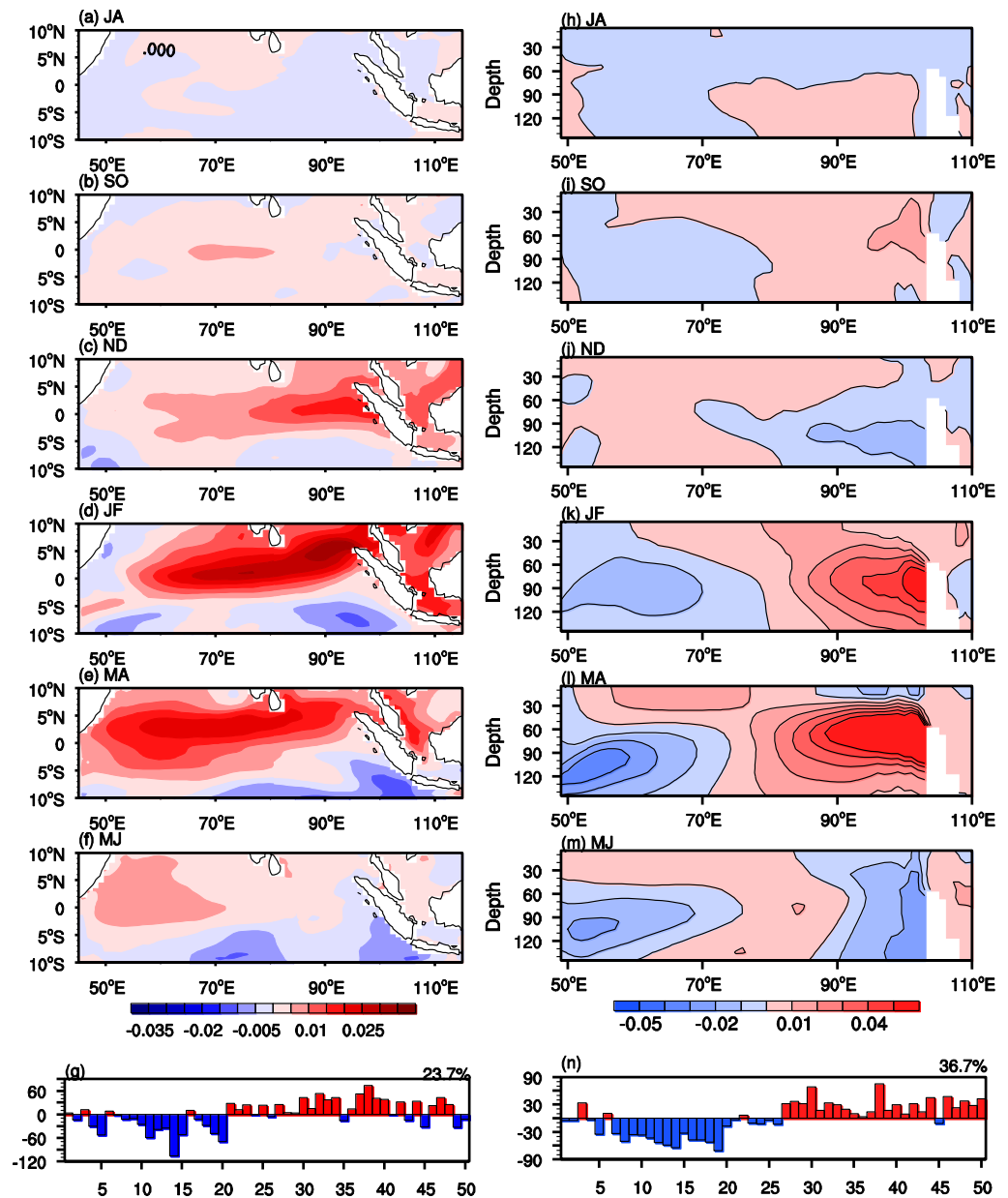
Figure 6. Major mode of time-dependent evolutions of (a–f) SST errors and (h–m) equatorial (5°S–5°N) subsurface temperature errors for 50 initial errors for start month July (−1) and July (0) (units: °C); (g and n) corresponding time series PC1. The numbers located on the horizontal axis in Figures 6g and 6n represent the 50 predictions with different initial errors. Each number corresponds to one prediction.

related initial errors, their dominant evolution mode and the corresponding time series (i.e., PC1) are shown in Figure 6. We found that the SST errors are weak in the first 2 months of the predictions, with negative SSTAs in the eastern Indian Ocean. Then, significant positive SST errors appear in the central-northeast Indian Ocean in November and December, and propagate westward to the western Indian Ocean in the following months. By conducting the heat flux analysis, it is found that the shortwave radiation and latent heat flux play an important role in the westward propagation of SST errors (not shown). The significant west-east dipole pattern in winter indicates that the prediction errors are large in winter, corresponding to the significant WPB. In the dominant evolution mode for vertical sections of sea temperature errors, positive (negative) temperature errors in the subsurface ocean lower (lift) the thermocline depth in the eastern (western) Indian Ocean and induce equatorial Rossby waves (Kelvin waves) which propagate westward (eastward) to the western (eastern) Indian Ocean. Specifically, positive subsurface temperature errors in the eastern Indian

Ocean propagate westward under the effects of equatorial Rossby waves in the first four patterns, which are followed by the negative subsurface temperature errors, finally resulting in a significant west-east dipole pattern in the subsurface ocean in winter with negative temperature errors in the western Indian Ocean and positive temperature errors in the eastern Indian Ocean.

As the time series PC1 shown in Figures 6g and 6n, the first 26 values of PC1 correspond to the WPB-related initial errors for start month July (-1), and the rest of the values correspond to the WPB-related initial errors for start month July (0). We found that most of the first 26 values in PC1 are negative, which indicates that the dominant evolution patterns of these WPB-related initial errors for start month July (-1) are opposite to these presented in Figure 6. Specifically, there are negative SST errors in the western Indian Ocean and positive SST errors in the eastern Indian Ocean in winter, which hinders the occurrence of the positive IOD in winter. In contrast, most of the rest of the values in PC1 are positive, which indicates that the dominant evolution modes of these initial errors are similar to the patterns shown in Figure 6. Therefore, there are positive SST errors in the western Indian Ocean and negative SST errors in the eastern Indian Ocean in winter, and this hinders the decay of the positive IOD in winter. Based on the above discussions, the WPB-related initial errors superimposed on the initial fields of the positive IOD for start month July (-1) (July (0)) usually hinder the occurrence (decay) of the positive IOD, resulting in large prediction errors in winter, and finally causing a significant WPB.

4. Implications of Similarities Between OPRs and OGEs in Targeted Observations

In section 3.1, using the CEOF analysis, we analyzed the dominant spatial patterns of precursors (i.e., the OPRs) and demonstrated that there are two main types of OPRs. The surface component of OPR-1 (OPR-2) is an indistinctive west-east dipole pattern, with a small area of negative (positive) signals to the coast of Sumatra and Java. Correspondingly, there is a significant west-east dipole pattern in the subsurface component, with positive (negative) signals in the western Indian Ocean and negative (positive) signals in the eastern Indian Ocean. In section 3.3, we revealed that there are also two types of OGEs, with a significant west-east dipole pattern in both the surface and subsurface components. It should be noted that the maximum values in the subsurface component are larger than those in the surface component for both the OPRs and OGEs, with the largest values located in the eastern equatorial Indian Ocean in the subsurface component. The above discussions naturally lead us to examine the spatial correlations between the OPRs and OGEs. To achieve this analysis, we calculated the similarities between the OPRs and OGEs using the following similarity coefficient:

$$r = \frac{\langle T^\alpha . T^\beta \rangle}{\|T^\alpha\|\|T^\beta\|} = \frac{\sum_{i=1}^{m}\sum_{j=1}^{n} T_{ij}^\alpha T_{ij}^\beta}{\sqrt{\sum_{i=1}^{m}\sum_{j=1}^{n}(T_{ij}^\partial)^2 \sum_{i=1}^{m}\sum_{j=1}^{n}(T_{ij}^\beta)^2}}, \quad (1)$$

where the fields of OPRs and OGEs are assumed to be vectors $T^\alpha = (T_{ij}^\alpha)_{m \times n}$ and $T^\beta = (T_{ij}^\beta)_{m \times n}$. T_{ij}^α and T_{ij}^β denote the values of sea temperature at grid point (i, j) in the tropical Indian Ocean (i.e., 10°S–10°N, 45°E–115°E). We computed the similarity coefficients between the OPRs and OGEs based on three aspects: the surface component, the subsurface component, and the two components together (Table 1). For simplicity, only the similarity coefficients between the OPR-1 and OGE-1 are shown. We found that the similarity coefficient for the surface component between the OPR-1 and OGE-1 for start month July (-1) is 0.56; and the similarity coefficient for the subsurface components is 0.89, which are larger than those for the surface component. Furthermore, the similarity coefficient for the surface and subsurface components together between the OPR-1 and OGE-1 for start month July (-1) is 0.74. This indicates that the similarity between the OPRs and OGEs is mainly reflected in the subsurface component, which represents a significant west-east dipole pattern, with the largest values located in the eastern equatorial Indian Ocean. These conclusions are also true for the other five start months. This may be closely related to the fact that the SST variability in the tropical Indian Ocean is dominated by the ENSO and subsurface variability is governed by the IOD [*Rao et al.*, 2002].

Based on the above discussions, the OPRs and OGEs have great spatial similarity and their large values are both concentrated within the small area of the eastern equatorial Indian Ocean in the subsurface component (i.e., 95 m depth) close to the thermocline depth. *Feng et al.* [2016] identified that these areas represent the sensitive areas of targeted observations for the positive IOD. By eliminating initial errors over these areas, the prediction errors in winter are largely reduced and the forecast skill is considerably improved. Therefore, in consideration of the spatial similarity between the OPRs and OGEs, if intensive observations are carried out

Table 1. The Correlation Coefficients Between the OPRs and OGEs From the Following Three Aspects: the Surface Component, the Subsurface Component, and the Two Components Together

Correlation Coefficients		OPRs		
		Surface	Subsurface	Surface and Subsurface
OGEs	July (−1) Surface	0.56		
	Subsurface		0.89	
	Surface and subsurface			0.74
	October (−1) Surface	0.10		
	Subsurface		0.91	
	Surface and subsurface			0.63
	January (0) Surface	0.45		
	Subsurface		0.95	
	Surface and subsurface			0.90
	April (0) Surface	0.70		
	Subsurface		0.98	
	Surface and subsurface			0.91
	July (0) Surface	0.80		
	Subsurface		0.95	
	Surface and subsurface			0.90
	October (0) Surface	0.46		
	Subsurface		0.91	
	Surface and subsurface			0.70

over these areas and assimilated into the initial fields, we can not only improve the accuracy of initial fields and decrease the prediction errors but also detect the precursory signals of the positive IOD in advance, which will substantially improve the forecast skill for the positive IOD.

5. Summary and Discussion

In this study, with the GFDL CM2p1, we explored the initial perturbations that are most likely to develop into positive IOD (i.e., precursors) and identified their dominant spatial patterns (i.e., OPRs). Furthermore, the dominant evolution patterns of these initial perturbations were analyzed using S-EOF analysis. Similarly, the initial errors that are most likely to cause a significant WPB (i.e., WPB-related initial errors) were also analyzed, as well as their dominant evolution patterns. The detailed results are as follows.

There are two main types of OPRs. The surface component of the OPR-1 (OPR-2) is an indistinctive west-east dipole pattern, with a small area of negative (positive) perturbations to the coast of the Sumatra and Java. Correspondingly, there is a significant west-east dipole pattern in the subsurface component of OPR-1 (OPR-2), with positive (negative) values in the western Indian Ocean and negative (positive) values in the eastern Indian Ocean. The largest values are located in the eastern equatorial Indian Ocean in the subsurface component (i.e., at 95 m depth). Based on S-EOF analysis, we explored the dominant mode of the time-dependent evolution for precursors. Both the evolution of the SSTAs and the vertical profile of sea temperatures in the tropical Indian Ocean bear close similarity to the development of the positive IOD. It needs to be highlighted that the spatial patterns of OPR-1 are similar to the precursor revealed in *Horii et al.* [2008], which suggests that another type of precursor exists in addition to the precursor identified by *Horii et al.* [2008].

Similarly, there are two types of OGEs (OGE-1 and OGE-2) that have opposite patterns. A significant west-east dipole pattern is present in both the surface component and subsurface components, with the largest values located in the eastern equatorial Indian Ocean in the subsurface component. The dominant evolution patterns for the SST errors present a westward propagation, during which the shortwave radiation and latent heat flux play an important role. They finally develop into a significant west-east dipole pattern in winter, which indicates a large prediction error in winter and corresponds to the WPB. The dominant evolution patterns for the vertical section of sea temperature errors propagate westward under the effects of equatorial Rossby waves. The WPB-related initial errors superimposed on the initial fields of positive IOD for start month July (−1) (July (0)) usually hinder the occurrence (decay) of the positive IOD, result in large prediction errors in winter, and finally cause a significant WPB.

Based on the above discussions, the OPRs and OGEs have great spatial similarity and their large values are both concentrated within a small area: the eastern equatorial Indian Ocean at 95 m depth. *Feng et al.* [2016] identified that such areas represent the sensitive areas of targeted observations for the positive IOD. Therefore, in consideration of the spatial similarity between the OPRs and OGEs, if intensive observations are carried out over these areas and assimilated into the initial fields, we cannot only improve the accuracy of initial fields and decrease the prediction errors but also detect the precursory signals of positive IOD in advance, which will considerably improve the forecast skill for the positive IOD. Of course, this hypothesis should be further verified using observing system simulation experiments (OSSEs) and observing system

experiments. *Luo et al.* [2007] stated that the Scale Interaction Experiment-Frontier Research Center for Global Change (SINTEX-F) failed to skillfully predict the cold signals in the eastern Indian Ocean in the 1997 IOD, which was mainly caused by the initial errors in the subsurface ocean in the tropical Indian Ocean. *Wajsowicz* [2005] also demonstrated that the poor initialization in the subsurface ocean will constrain the forecast skill for predicting the IOD. These results further emphasize that intensive observations should be carried out in the subsurface ocean in the tropical Indian Ocean, which is consistent with the results in this study.

The similarities between OPRs and OGEs of atmospheric and oceanic events are one of interesting issues in the predictability studies. Based on the CNOP approach [*Mu et al.*, 2003], the OPRs and OGEs of ENSO [*Mu et al.*, 2014] and KLM [*Wang et al.*, 2013] have been explored and the results demonstrated that the OPRs and OGEs have great spatial similarities. This provides valuable information regarding the sensitive areas of targeted observations for ENSO and KLM. Because of the lack of adjoint models in the GFDL CM2p1, we obtained the OPRs and OGEs of IOD by using the ensemble-based method in *Duan et al.* [2009]. These disturbances were identified from the sea temperature anomalies within the 4 years preceding the reference year (i.e., neutral year or IOD year). However, this strategy may not guarantee that the constructed initial perturbations encompass all kinds of initial patterns. Therefore, the OPRs and OGEs obtained in the present study may only approximate the theoretical disturbances. More effective algorithms are expected to be developed to compute CNOP of high-dimensional models, and calculate the OPRs and OGEs in complex models.

References

Abram, N. J., M. K. Gagan, M. T. McCulloch, J. Chappell, and W. S. Hantoro (2003), Coral reef death during the 1997 Indian Ocean dipole linked to Indonesian wildfires, *Science*, *301*(5635), 952–955.

Annamalai, H., and R. Murtugudde (2004), Role of the Indian Ocean in regional climate variability, *Earth Clim. Ocean Atmos. Interact.*, 147, 213–246.

Ansell, T., C. J. C. Reason, and G. Meyers (2000), Variability in the tropical southeast Indian Ocean and links with southeast Australian winter rainfall, *Geophys. Res. Lett.*, *27*(24), 3977–3980.

Ashok, K., Z. Guan, and T. Yamagata (2001), Impact of the Indian Ocean dipole on the relationship between the Indian monsoon rainfall and ENSO, *Geophys. Res. Lett.*, *28*(23), 4499–4502.

Ashok, K., Z. Guan, and T. Yamagata (2003), Influence of the Indian Ocean dipole on the Australian winter rainfall, *Geophys. Res. Lett.*, *30*(15), 1821, doi:10.1029/2003GL017926.

Behera, S. K., J. J. Luo, S. Masson, P. Delecluse, S. Gualdi, A. Navarra, and T. Yamagata (2005), Paramount impact of the Indian Ocean dipole on the East African short rains: A CGCM study, *J. Clim.*, *18*(21), 4514–4530.

Bjerknes, J. (1969), Atmospheric teleconnections from the equatorial pacific, *Mon. Weather Rev.*, *97*(3), 163–172.

Black, E., J. Slingo, and K. R. Sperber (2003), An observational study of the relationship between excessively strong short rains in coastal east Africa and Indian Ocean SST, *Mon. Weather Rev.*, *131*(1), 74–94.

Cai, W., T. Cowan, and A. Sullivan (2009), Recent unprecedented skewness towards positive Indian Ocean Dipole occurrences and its impact on Australian rainfall, *Geophys. Res. Lett.*, *36*, L11705, doi:10.1029/2009GL037604.

Dai, G., M. Mu, and Z. Jiang (2016), Relationships between optimal precursors triggering NAO onset and optimally growing initial errors during NAO prediction, *J. Atmos. Sci.*, *73*, 293–317, doi:10.1175/JAS-D-15-0109.1.

Duan, W., X. Liu, K. Zhu, and M. Mu (2009), Exploring the initial errors that cause a significant "spring predictability barrier" for El Niño events, *J. Geophys. Res.*, *114*, C04022, doi:10.1029/2008JC004925.

Feng, M., and G. Meyers (2003), Interannual variability in the tropical Indian Ocean: A two-year time-scale of Indian Ocean Dipole, *Deep Sea Res., Part II*, *50*, 2263–2284.

Feng, R., and W. S. Duan (2014), The spatial patterns of initial errors related to the "winter predictability barrier" of the Indian Ocean dipole, *Atmos. Oceanic Sci. Lett.*, *7*, 406–410, doi:10.3878/j.issn.1674-2834.14.0018.

Feng, R., W. S. Duan, and M. Mu (2014a), The "winter predictability barrier" for IOD events and its error growth dynamics: Results from a fully coupled GCM, *J. Geophys. Res. Oceans*, *119*, 8688–8708, doi:10.1002/2014JC010473.

Feng, R., M. Mu, and W. S. Duan (2014b), Study on the "winter persistence barrier" of Indian Ocean dipole events using observation data and CMIP5 model outputs, *Theor. Appl. Climatol.*, *118*(3), 523–534, doi:10.1007/s00704-013-1083-x.

Feng, R., W. S. Duan, and M. Mu (2016), Estimating observing locations for advancing beyond the winter predictability barrier of Indian Ocean dipole event predictions, *Clim. Dyn.*, doi:10.1007/s00382-016-3134-3.

GFDL Global Atmospheric Model Development Team (2004), The new GFDL global atmosphere and land model AM2–LM2: Evaluation with prescribed SST simulations, *J. Clim.*, *17*, 4641–4673.

Griffies, S. M. (2009), Elements of MOM4p1: GFDL ocean group, *Tech. Rep. 6*, NOAA/Geophys. Fluid Dyn. Lab., Princeton, N. J.

Guan, Z., and T. Yamagata (2003), The unusual summer of 1994 in East Asia: IOD teleconnections, *Geophys. Res. Lett.*, *30*(10), 1544, doi:10.1029/2002GL016831.

Horii, T., H. Hase, I. Ueki, and Y. Masumoto (2008), Oceanic precondition and evolution of the 2006 Indian Ocean dipole, *Geophys. Res. Lett.*, *35*, L03607, doi:10.1029/2007GL032464.

Hu, J., and W. Duan (2016), Relationship between optimal precursory disturbances and optimally growing initial errors associated with ENSO events: Implications to target observations for ENSO prediction, *J. Geophys. Res. Oceans*, *121*, 2901–2917, doi:10.1002/2015JC011386.

Li, T., Y. Zhang, E. Lu, and D. Wang (2002), Relative role of dynamic and thermodynamic processes in the development of the Indian Ocean dipole: An OGCM diagnosis, *Geophys. Res. Lett.*, *29*(23), 2110, doi:10.1029/2002GL015789.

Li, T., B. Wang, C. P. Chang, and Y. Zhang (2003), A theory for the Indian Ocean dipole–zonal mode, *J. Atmos. Sci.*, *60*(17), 2119–2135.

Liu, H. F., Y. M. Tang, D. Chen, and T. Lian (2016), Predictability of the Indian Ocean Dipole in the coupled models, *Clim. Dyn.*, doi:10.1007/s00382-016-3187-3.

Luo, J. J., S. Masson, S. Behera, S. Shingu, and T. Yamagata (2005), Seasonal climate predictability in a coupled OAGCM using a different approach for ensemble forecasts, *J. Clim.*, *18*(21), 4474–4497.

Luo, J. J., S. Masson, S. Behera, and T. Yamagata (2007), Experimental forecasts of the Indian Ocean dipole using a coupled OAGCM, *J. Clim.*, *20*(10), 2178–2190, doi:10.1175/JCLI4132.1.

Mu, M., and Z. Jiang (2011), Similarities between optimal precursors that trigger the onset of blocking events and optimally growing initial errors in onset prediction, *J. Atmos. Sci.*, *68*, 2860–2877.

Mu, M., W. Duan, and B. Wang (2003), Conditional nonlinear optimal perturbation and its applications, *Nonlinear Process Geophys.*, *10*(6), 493–501, doi:10.5194/npg-10-493-2003.

Mu, M., Y. Yu, H. Xu, and T. Gong (2014), Similarities between optimal precursors for ENSO events and optimally growing initial errors in El Niño predictions, *Theor. Appl. Climatol.*, *115*, 461–469, doi:10.1007/s00704-013-0909-x.

Philander, S. G. H. (1983), El Niño southern oscillation phenomena, *Nature*, *302*(5906), 295–301.

Philander, S. G. H. (1990), *El Niño, La Niña and the Southern Oscillation*, 293 pp., Academic, San Diego, Calif.

Rao, A. S., S. K. Behera, Y. Masumoto, and T. Yamagata (2002), Interannual variability in the subsurface Indian Ocean with special emphasis on the Indian Ocean Dipole, *Deep Sea Res., Part II*, *49*, 1549–1572.

Rasmusson, E. M., and T. H. Carpenter (1982), Variations in tropical sea surface temperature and surface wind fields associated with the Southern Oscillation/El Niño, *Mon. Weather Rev.*, *110*(5), 354–384.

Saji, N. H., and T. Yamagata (2003), Interference of teleconnection patterns generated from the tropical Indian and Pacific Oceans, *Clim. Res.*, *25*, 151–169.

Saji, N. H., B. N. Goswami, P. N. Vinayachandran, and T. Yamagata (1999), A dipole mode in the tropical Indian Ocean, *Nature*, *401*(6751), 360–363.

Shi, L., H. H. Hendon, O. Alves, J. J. Luo, M. Balmaseda, and D. Anderson (2012), How predictable is the Indian Ocean dipole?, *Mon. Weather Rev.*, *140*(12), 3867–3884, doi:10.1175/MWR-D-12-00001.1.

Song, Q., G. A. Vecchi, and A. J. Rosati (2007), Indian Ocean variability in the GFDL Coupled Climate Model, *J. Clim.*, *20*, 2895–2916, doi:10.1175/JCLI4159.1.

Vinayachandran, P. N., S. Iizuka, and T. Yamagata (2002), Indian Ocean dipole mode events in an ocean general circulation model, *Deep Sea Res., Part II*, *49*(7), 1573–1596.

Wajsowicz, R. C. (2004), Climate variability over the tropical Indian Ocean sector in the NSIPP seasonal forecast system, *J. Clim.*, *17*(24), 4783–4804.

Wajsowicz, R. C. (2005), Potential predictability of tropical Indian Ocean SST anomalies, *Geophys. Res. Lett.*, *32*, L24702, doi:10.1029/2005GL024169.

Wang, B., and S. I. An (2005), A method for detecting season-dependent modes of climate variability: S-EOF analysis, *Geophys. Res. Lett.*, *32*, L15710, doi:10.1029/2005GL022709.

Wang, Q., M. Mu, and H. A. Dijkstra (2013), The similarity between optimal precursor and optimally growing initial error in prediction of Kuroshio large meander and its application to targeted observation, *J. Geophys. Res. Oceans*, *118*, 869–884, doi:10.1002/jgrc.20084.

Webster, P. J., A. M. Moore, J. P. Loschnigg, and R. R. Leben (1999), Coupled ocean-atmosphere dynamics in the Indian Ocean during 1997-1998, *Nature*, *401*(6751), 356–360.

Weller, E., and W. Cai (2013), Asymmetry in the IOD and ENSO teleconnection in a CMIP5 model ensemble and its relevance to regional rainfall, *J. Clim.*, *26*, 5139–5149.

Zhang, L., F. Sielmann, K. Fraedrich, X. H. Zhu, and X. F. Zhi (2015), Variability of winter extreme precipitation in Southeast China: Contributions of SST anomalies, *Clim. Dyn.*, *45*, 2557–2570, doi:10.1007/s00382-015-2492-6.

Zhao, M., and H. H. Hendon (2009), Representation and prediction of the Indian Ocean dipole in the POAMA seasonal forecast model, *Q. J. R. Meteorol. Soc.*, *135*(639), 337–352, doi:10.1002/qj.370.

Zubair, L., A. S. Rao, and T. Yamagata (2003), Modulation of Sri Lankan Maha rainfall by the Indian Ocean dipole, *Geophys. Res. Lett.*, *30*(2), 1063, doi:10.1029/2002GL015639.